Transactions of Tianjin University (2019) 25:340–347
https://doi.org/10.1007/s12209-019-00202-1

RESEARCH ARTICLE

Ni-Doped $BiVO_4$ with V^{4+} Species and Oxygen Vacancies for Efficient Photoelectrochemical Water Splitting

Dechao Kong[1,2,3] · Jie Qi[1,2,3] · Danyang Liu[4] · Xiangwen Zhang[1,2,3] · Lun Pan[1,2,3] · Jijun Zou[1,2,3]

Received: 5 March 2019 / Revised: 29 March 2019 / Accepted: 14 April 2019 / Published online: 18 May 2019

Abstract

Bismuth vanadate is a promising photoanode material for photoelectrochemical (PEC) water splitting, but its activity and stability need to be further improved. In this work, we synthesized Ni-doped $BiVO_4$ abundant with V^{4+} species and oxygen defects through an in situ electrodeposition method. The effective doping can decrease the particle size of $BiVO_4$ and lead to the formation of V^{4+} species/oxygen defects. Accordingly, the doped and defective $BiVO_4$ showed high optical absorption and rapid charge transfer, and further showed much higher PEC activity than pure $BiVO_4$. Specifically, 5-Ni-$BiVO_4$ exhibits the highest activity in PEC water splitting, with a photocurrent of 2.39 mA/cm^2 at 1.23 V versus RHE (the reversible hydrogen electrode), which is 2.5 times higher than pure $BiVO_4$ (0.94 mA/cm^2), and much higher incident photon-to-current efficiency (IPCE) value of 45% (while only 25% for $BiVO_4$ at ca. 400 nm). This work provides an in situ method for the development of a high-performance photoanode.

Keywords $BiVO_4$ · Doping · Photoelectrochemistry · V^{4+} species · Oxygen vacancies

Introduction

As the energy crisis and environmental pollution have become serious issues in the past decades [1], sustainable energy needs to be explored, and the utilization of solar energy has drawn much attention recently [2–4]. Specifically, photoelectrochemical (PEC) water splitting has been regarded as a promising pathway to convert solar energy to hydrogen fuel [5].

Since Fujishima and Honda [6] first applied TiO_2 as a photoanode material for PEC water splitting, much research has been carried out to explore the active photoanodes, such as WO_3, Fe_2O_3, ZnO, $BiVO_4$ [7–12]. Among them, bismuth vanadate (m-$BiVO_4$) is an ideal material, attributed to its suitable band gap of 2.4 eV [13–16] and the ideal PEC current density of 7.6 mA/cm^2 under solar light [11].

However, the rapid recombination of the photo-induced electron–hole pairs in $BiVO_4$ restricts its PEC properties. Recently, several methods have been applied to improve its PEC performance, such as morphology control [15, 16], heterojunction [17–20], surface modification [12, 21], and element doping [22–27]. Among them, doping by metal ions is a promising approach to tune the electronic and band structures, which may also cause surface defects and further improve the charge separation [26–31]. Recently, Ni ions were applied to narrow the band gap of $BiVO_4$ [32–35], and the atom radii difference between Ni^{2+} (0.78 Å) and Bi^{3+} (1.03 Å) could lead to abundant surface defects, which are beneficial to optical absorption and charge transfer [36].

Dechao Kong and Jie Qi have contributed equally to this work.

Electronic supplementary material The online version of this article (https://doi.org/10.1007/s12209-019-00202-1) contains supplementary material, which is available to authorized users.

✉ Lun Pan
panlun76@tju.edu.cn

✉ Jijun Zou
jj_zou@tju.edu.cn

1 Key Laboratory for Green Chemical Technology of the Ministry of Education, Tianjin University, Tianjin 300072, China

2 School of Chemical Engineering and Technology, Tianjin University, Tianjin 300350, China

3 Collaborative Innovation Center of Chemical Science and Engineering (Tianjin), Tianjin University, Tianjin 300072, China

4 People's Public, Security University of China, Beijing 100038, China

In this work, we used an in situ electrodeposition method to fabricate a Ni-doped $BiVO_4$ photoanode for PEC water splitting. The doping of Ni ions into the $BiVO_4$ lattice decreases the particle size and causes abundant V^{4+} species and oxygen defects, which shorten the migration length of charge carriers and enhance optical absorption. Therefore, 5-Ni-$BiVO_4$ exhibits very high PEC performance, with a photocurrent of 2.39 mA/cm^2 at 1.23 V versus RHE (the reversible hydrogen electrode) and an incident photon-to-current conversion efficiency (IPCE) value of 45% (at 400 nm).

Experimental Section

Materials

$Bi(NO_3)_3{\cdot}H_2O$, $Ni(NO_3)_2{\cdot}6H_2O$, $VO(acac)_2$, KI, *p*-benzoquinone, KOH, and absolute ethanol were all obtained from Aladdin Chemicals Co., Ltd. (China). Dimethyl sulfoxide (DMSO) and HNO_3 were purchased from Tianjin Jiangtian Chemical Institute. Milli-Q ultrapure water (> 18 mΩ/cm) was used in all experiments. All reagents were of analytical grade and used without further purification.

Synthesis of Doped $BiVO_4$

0.4 mol/L KI solution (pH = 1.7), $Bi(NO_3)_3{\cdot}H_2O$ (0.97 g), and $Ni(NO_3)_2{\cdot}6H_2O$ (0%, 3%, 5%, 10% of Bi source) were dissolved in ultrapure water, which was then mixed with 20 mL of absolute ethanol containing 0.497 g *p*-benzoquinone (as an electrolyte). Then, a piece of fluorine-doped tin oxide (FTO), a saturated Ag/AgCl electrode, and a platinum counter were used as a working electrode, reference electrode, and counter electrode in a three-electrode cell for electrodeposition, respectively. The electrodeposition of BiOI electrode was then operated potentiostatically at − 0.1 V versus Ag/AgCl for 3 min.

Then, 0.14 mL of DMSO solution containing 0.106 g $VO(acac)_2$ was dripped on the BiOI electrode, which was dried in a vacuum at 40 °C for 8 h. Afterward, the electrodes were calcined at 450 °C for 2 h with an increasing rate of 2 °C/min to obtain $BiVO_4$. Then, 1.0 mol/L KOH was used to rinse the surface V_2O_5. The Ni-doped $BiVO_4$ with varied proportions was named as 3-Ni-$BiVO_4$, 5-Ni-$BiVO_4$, and 10-Ni-$BiVO_4$.

Characterization

X-ray diffraction (XRD) characterization was applied to analyze the crystalline phase of samples with a diffractometer by Germany Brooke AXSCO. A field emission scanning electron microscope (FE-SEM, Hitachi S-4800) was used to investigate the morphology. High-resolution transmission electron microscopy (HR-TEM, Tecnai G^2 F-20) and the attached energy dispersive spectrometer (EDS) were applied to obtain the microstructures and the elemental distribution. The X-ray photoelectron spectrum (XPS) was used to characterize the surface composition of samples, which was conducted with a PHI-1600 X-ray photoelectron spectroscope equipped with Al Kα radiation. Raman spectra were carried out with a Raman spectrometer (DXR Microscope), and the excitation source was a green semiconductor laser (532 nm). Steady-state photoluminescence (PL) spectra were measured by a Horiba Jobin–Yvon Fluorolog 3-21 with the excitation light at 420 nm. The UV–Vis diffuse reflectance spectra (UV–Vis DRS) were recorded on a Shimadzu U-2600 spectrometer equipped with a 60-mm-diameter integrating sphere of $BaSO_4$. The concentration of Ni was detected by inductively coupled plasma-mass spectrometry (ICP-MS) (ICP-MS XSERIES 2, Thermo Fisher Scientific).

PEC Tests

A typical three-electrode cell and a CHI 660E electrochemical workstation were applied to evaluate the PEC performance of the $BiVO_4$-based photoanodes. The simulated solar illumination source was a 300 W Xe arc lamp (100 mW/cm^2, PLS-SXE300UV, Beijing Trusttech. Co. Ltd). The electrolyte for the photocurrent measurements was a 0.2 mol/L Na_2SO_4 aqueous solution. Linear sweep voltammetry (LSV) was monitored while sweeping the potential to the positive direction with a scan rate of 10 mV/s. The potential versus Ag/AgCl reference electrode was converted to the reversible hydrogen electrode (RHE) according to the Nernst equation: E (vs. RHE) = E (vs. Ag/AgCl) + 0.0591 pH + 0.197. Electrochemical impedance spectroscopy (EIS) measurement was taken with a sinusoidal ac perturbation of 10 mV applied over the frequency range of 0.1–10^5 Hz.

Moreover, the IPCE was then determined and calculated as follows [37]:

$$\mathrm{IPCE}\,(\lambda) = \frac{1240J\,(\lambda)}{P\,(\lambda)} \times 100\% \quad (1)$$

where λ is the wavelength (nm), $J(\lambda)$ is the photocurrent density (mA/cm^2), and $P(\lambda)$ is the incident power density of the monochromatic light (mW/cm^2).

Results and Discussion

Crystal Structure and Morphology

As shown in Fig. 1a, pure $BiVO_4$ and Ni-doped $BiVO_4$ samples all showed the typical diffraction peaks of monoclinic

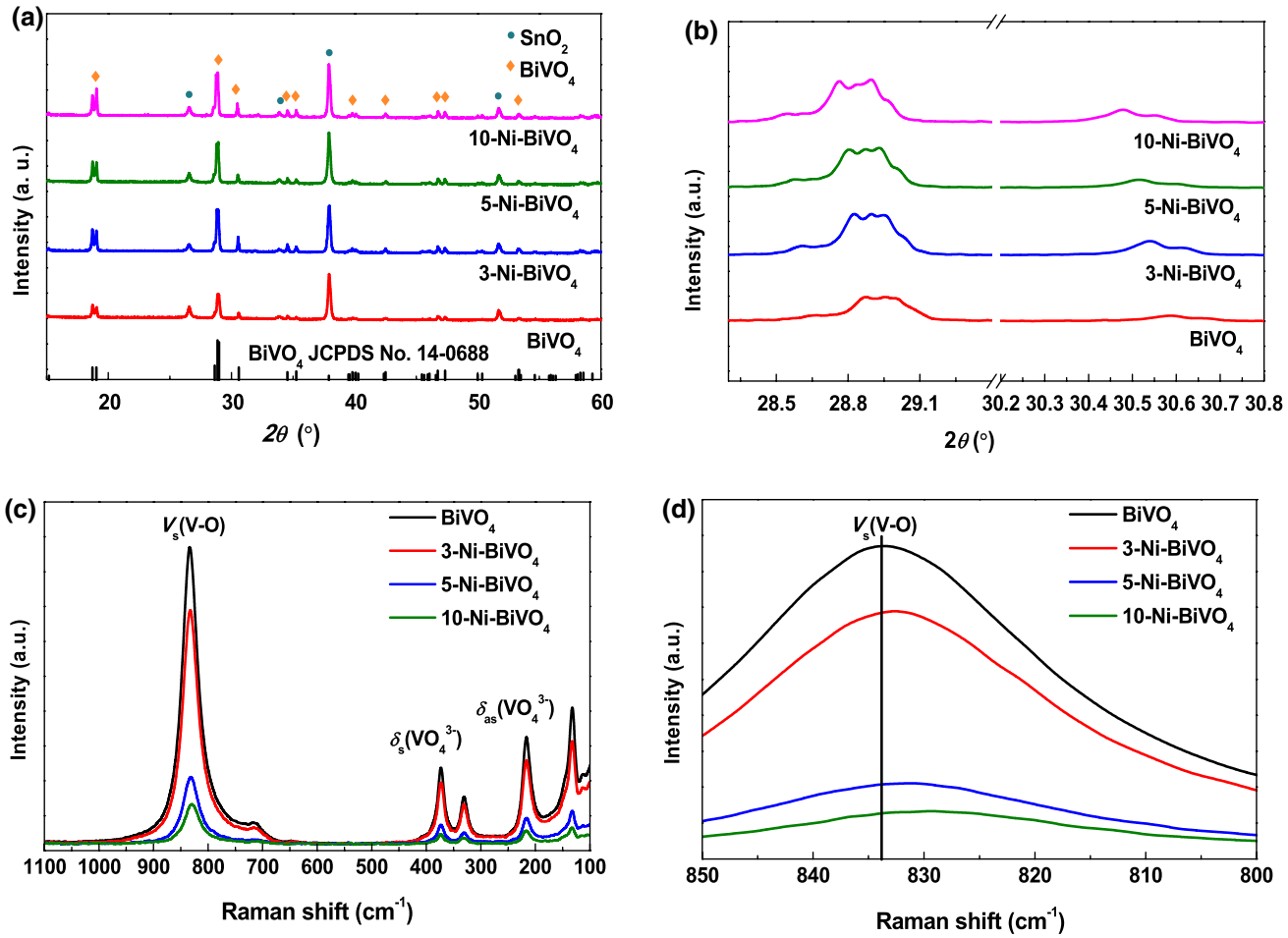

Fig. 1 **a**, **b** XRD patterns and **c, d** Raman spectra of $BiVO_4$ and Ni-doped $BiVO_4$ samples

scheelite $BiVO_4$ (JCPDS No. 14-0688, space group 15, C_{2h}), with other peaks referring to FTO glass (SnO_2, JCPDS No. 41-1445), indicating the absence of nickel oxide species. As shown in the magnified spectra (Fig. 1b), the left shift of the diffraction peak should be owing to the substitution of Bi sites by Ni cations [38], indicating the effective Ni doping in $BiVO_4$.

In the Raman spectra (Fig. 1c), the characteristic vibration peaks of all samples refer to the crystal structure of monoclinic scheelite $BiVO_4$, and the Ni doping gradually decreased the crystallization of $BiVO_4$, which may have caused surface defects. The peak at 215.9 cm^{-1} was attributed to the external vibration of $BiVO_4$. The peaks at 330.6 cm^{-1} and 373.1 cm^{-1} were caused by V–O asymmetrical vibration and V–O bending vibration in the VO_4^{3-} unit, while the peaks at 717 and 834.0 cm^{-1} could be attributed to two different modes of stretching vibration of V–O [39–42]. Ni-$BiVO_4$ samples showed similar Raman peaks with $BiVO_4$, but the band position at 834.0 cm^{-1} right-shifted gradually with increasing Ni doping concentration (Fig. 1d), indicating the gradual deformation of VO_4^{3-} [43]. This should be caused by the much smaller atomic radius of doped Ni^{2+} (0.78 Å) rather than Bi^{3+} (1.03 Å), leading to the crystal deformation and surface defects.

SEM images of BiOI, pure $BiVO_4$, and Ni-doped $BiVO_4$ samples are shown in Fig. 2a–e. The BiOI crystals, with or without Ni, had similar structures of thin two-dimensional nanoflakes (Fig. 2a, Fig. S1 in Supporting Information), which was beneficial for V precursor diffusion to produce $BiVO_4$. However, the Ni doping made BiOI structures much denser (Fig. S1), benefiting the crystal size decrease in the produced $BiVO_4$ [18]. After thermal calcination, all samples possessed the sponge-like network film with a thickness of ca. 1 μm (Fig. 2b–e). And, compared with pure $BiVO_4$, Ni doping decreased the size of $BiVO_4$ nanoparticles, and higher Ni content led to smaller crystal sizes ($BiVO_4$, 500 nm; 3-Ni-$BiVO_4$, 440 nm; 5-Ni-$BiVO_4$, 310 nm; 10-Ni-$BiVO_4$, 200 nm). The contractible particle might have enhanced the separation efficiency of the photo-induced charges [44]. Figure 2f shows the typical nanoparticle stacking structure of doped $BiVO_4$ (5-Ni-$BiVO_4$), which assembled the sponge-like network of $BiVO_4$. From

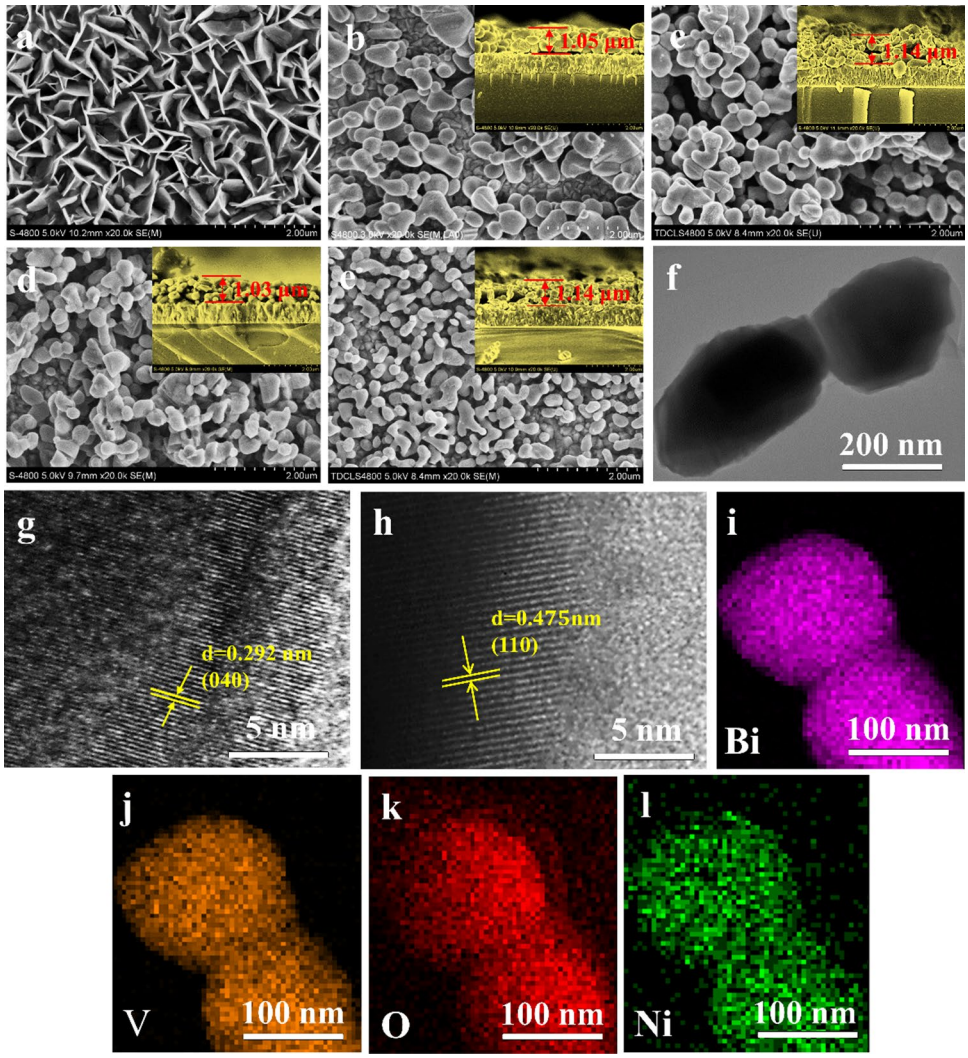

Fig. 2 SEM images of **a** BiOI, **b** $BiVO_4$, **c** 3-Ni-$BiVO_4$, **d** 5-Ni-$BiVO_4$, **e** 10-Ni-$BiVO_4$, **f** TEM, **g, h** HR-TEM, and **i–l** EDS mapping images of 5-Ni-$BiVO_4$

HR-TEM images (Fig. 2g, h), the lattice fringes with intervals of 0.475 nm and 0.292 nm corresponded to the (110) and (040) planes of the $BiVO_4$, respectively. As shown in EDS mapping (Fig. 2i–l), the uniform Ni distribution in the $BiVO_4$ proves that Ni species are successfully doped in the lattice. ICP data (Table S1) indicated that the content of Ni rose gradually from 3-Ni-$BiVO_4$ to 10-Ni-$BiVO_4$.

Chemical State

The chemical states of $BiVO_4$ and Ni-$BiVO_4$ samples were detected by XPS. The binding energies of Bi $4f_{7/2}$ at 159 eV and Bi $4f_{5/2}$ at 164.3 eV were assigned to Bi^{3+} species (Fig. 3a), while the V $2p_{1/2}$ and V $2p_{3/2}$ peaks of $BiVO_4$ located at 523.8 eV and 516.5 eV referred to V^{5+} species (Fig. 3b). But for Ni-$BiVO_4$, the obvious asymmetric peak of V $2p_{3/2}$ confirmed the existence of V^{4+} species (516.1 eV) (related to oxygen vacancies) [45]. Furthermore, the Bi 4*f* peaks of Ni-$BiVO_4$ all shifted to lower binding energies compared to pure $BiVO_4$, owing to the lower electronegativities of Ni^{2+} than Bi^{3+} via the Bi-O-Ni connection [35, 38]. In addition, the doping of Ni resulted in the presence of oxygen vacancies, which also led to the obvious red shift of Bi 4*f* [16].

It is worth noting that the concentrations of V^{4+} species and oxygen vacancies increased with the doping concentration, but stayed constant when the doping concentration was $\geq 5\%$. From Fig. 3d, the binding energies of the dominant Ni 2*p* XPS peaks were found to locate at 855.7, 861.3, 873.6 and 879.8 eV, and contributed to the Ni $2p_{3/2}$ main peak, Ni $2p_{1/2}$ main peak, Ni $2p_{3/2}$ satellite peak, and Ni $2p_{1/2}$ satellite peak, respectively. The peak intensity strengthened with the amount of Ni doping, confirming the effective Ni doping in the $BiVO_4$ lattice. The decreasing concentration of free electrons in Ni-$BiVO_4$ has been reported to stabilize the oxygen defects [46].

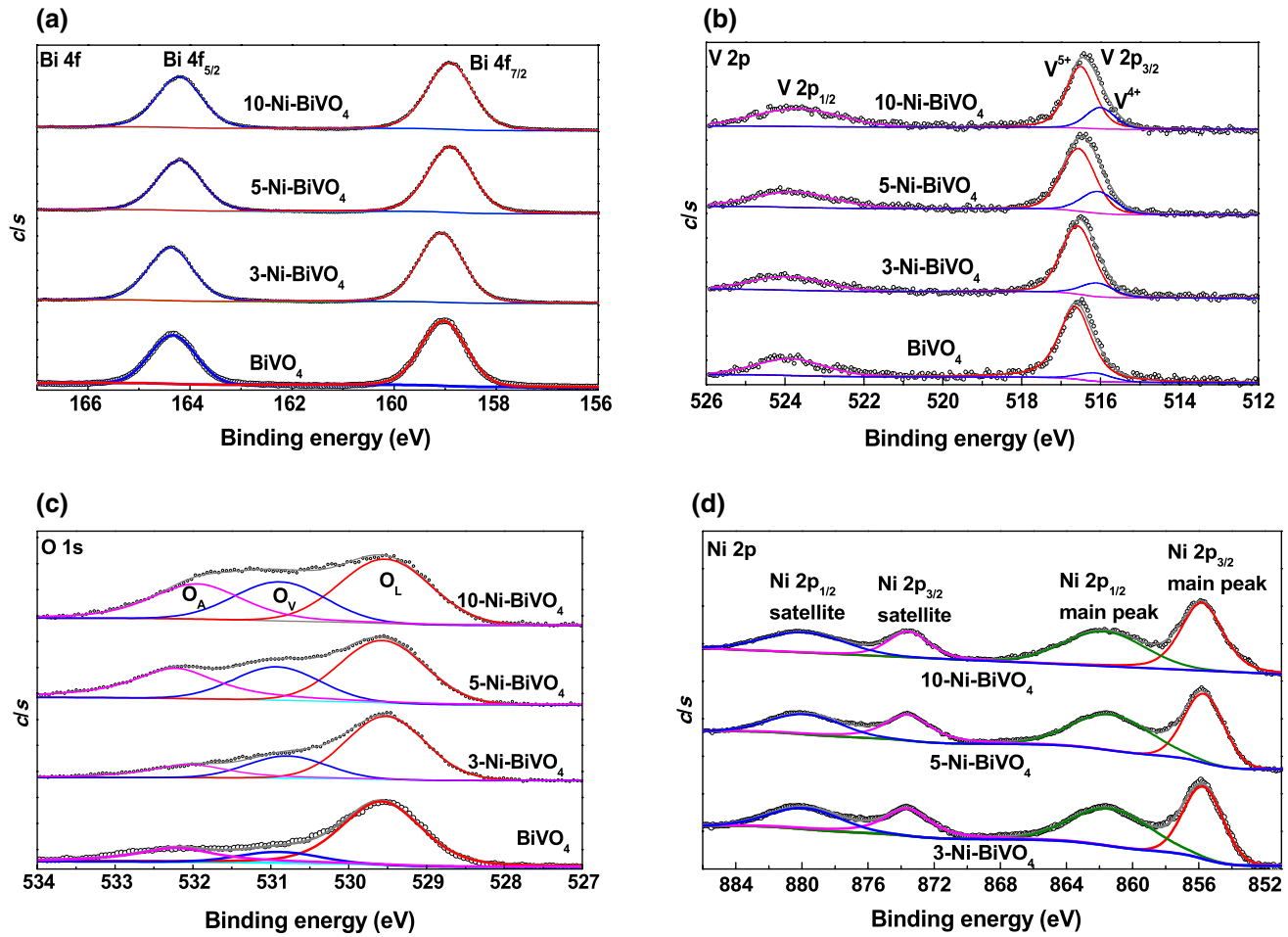

Fig. 3 XPS spectra of $BiVO_4$ and Ni-$BiVO_4$ samples. **a** Bi 4*f*, **b** V 2*p*, **c** O 1*s*, **d** Ni 2*p*

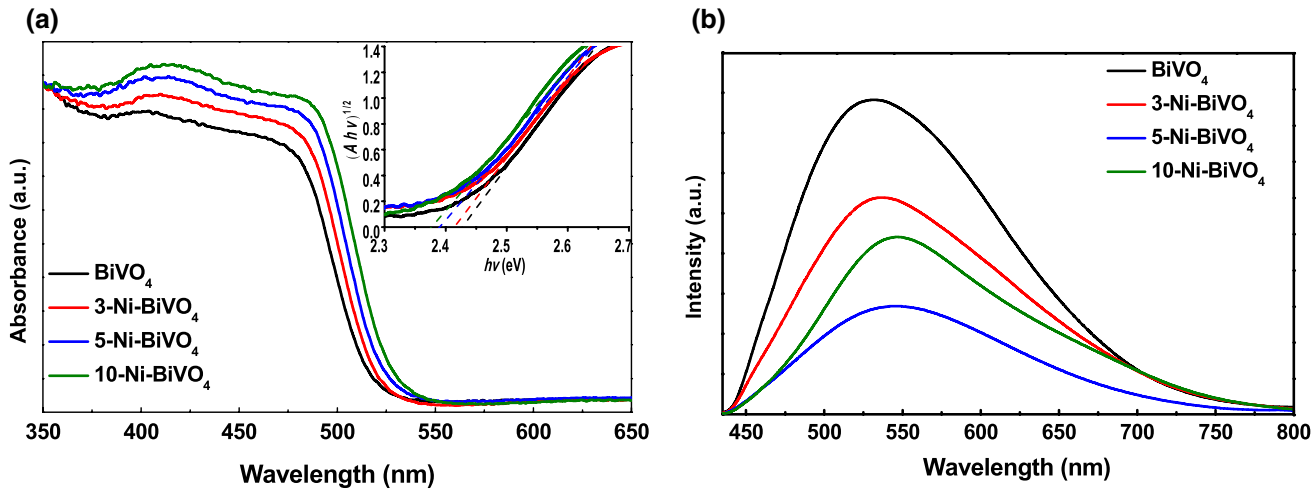

Fig. 4 UV–Vis absorption **a** and PL spectra **b** of $BiVO_4$ and Ni-doped $BiVO_4$

Optical Properties

The optical absorption spectra were analyzed and are shown in Fig. 4a. The absorption band edge of pure $BiVO_4$ is at about 530 nm, corresponding to its bandgap. Importantly, Ni doping led to stronger absorption intensity and a red shift of the absorption edge, which was enhanced gradually with the increase in Ni concentration.

According to the absorption spectrum, the band gap of samples was calculated as follows:

$$\alpha h\nu = A\left(h\nu - E_g\right)^n \quad (2)$$

where α, $h\nu$, A, E_g, and n are the absorption coefficient, photon energy, proportionality constant, band gap energy, and a coefficient, respectively. Since $BiVO_4$ was an indirect band gap material, the n value was 2.

As shown in Fig. 4a, the band gap of $BiVO_4$ was ca. 2.43 eV, while those of Ni-doped $BiVO_4$ were 2.42 eV for 3-Ni-$BiVO_4$, 2.39 eV for 5-Ni-$BiVO_4$, and 2.38 eV for 10-Ni-$BiVO_4$. The decrease in band gap should be attributed to the introduced band levels of Ni-doping-mediated V^{4+} species and oxygen defects.

Photoluminescence (PL) spectra were performed to investigate the charge carrier recombination. As shown in Fig. 4b, the main emission peaks of all samples were at ca. 530 nm, for the recombination of extrinsic radiative transitions [16]. Notably, Ni-doped $BiVO_4$ samples exhibited a lower emission peak intensity than $BiVO_4$, suggesting that the recombination of charge pairs was inhibited and more holes transferred to the surface to trigger the water oxidation reaction [47]. However, too many dopants (10-Ni-$BiVO_4$) lead to an increase in emission peak intensity, attributed to the fact that part of the foreign Ni species acts at the recombination sites and suppresses the PEC performance [33].

PEC Performance

PEC performance of the samples was examined under AM 1.5 G (100 mW/cm^2), and the results are shown in Fig. 5a. Under a dark environment, no photocurrent could be observed for $BiVO_4$, while it showed a photocurrent of

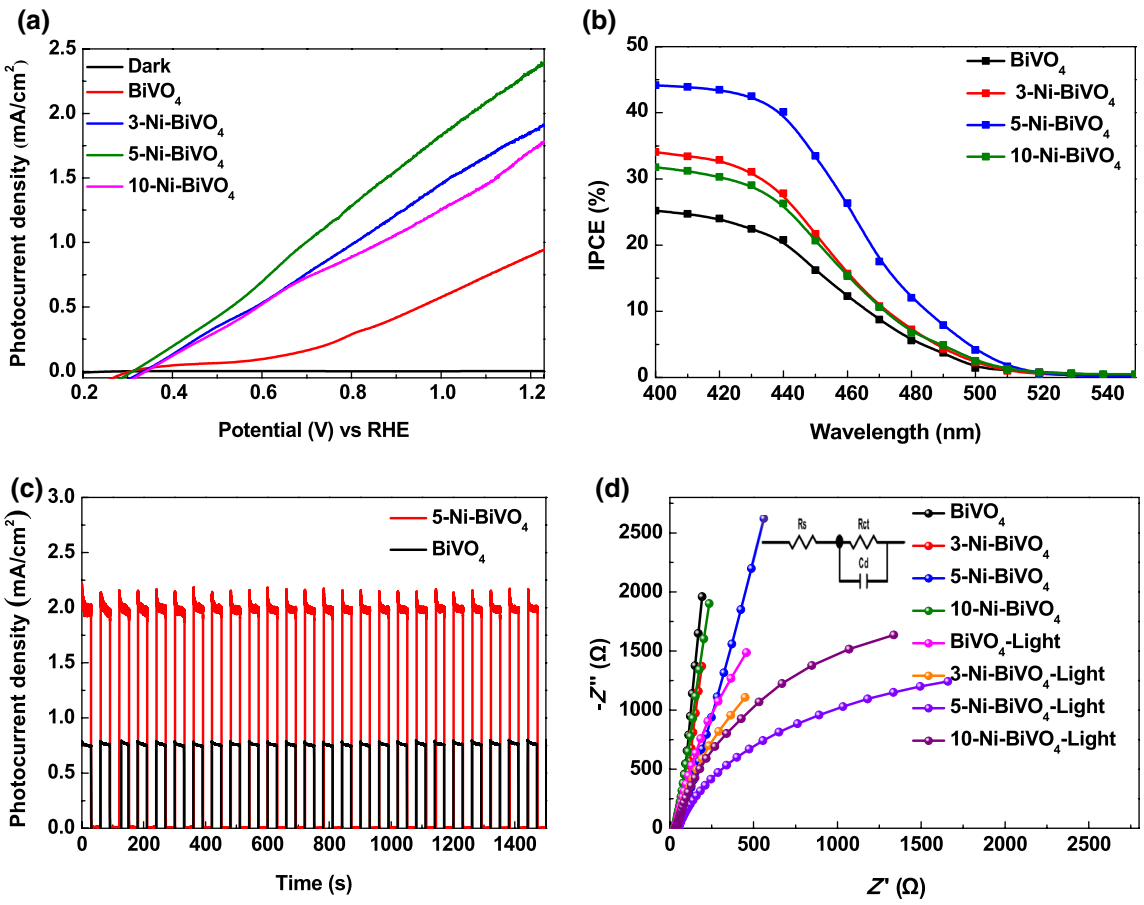

Fig. 5 **a** J–V curves of pure $BiVO_4$ and Ni-doped $BiVO_4$, **b** IPCE at 1.1 V versus RHE, **c** PEC stability of 5-Ni-$BiVO_4$ and pure $BiVO_4$ at 1.1 V versus RHE, and **d** EIS with and without light

0.94 mA/cm^2 at 1.23 V versus RHE under light irradiation. Importantly, the Ni doping could significantly improve the PEC performance, i.e., 1.91 mA/cm^2 (1.23 V vs. RHE) for 3-Ni-$BiVO_4$. Particularly, 5-Ni-$BiVO_4$ showed the highest photocurrent of 2.39 mA/cm^2 (1.23 V vs. RHE), which was 2.5 times higher than pure $BiVO_4$. However, further increasing the Ni doping amount resulted in a decrease in PEC performance, i.e., 1.73 mA/cm^2 for 10-Ni-$BiVO_4$, because the excess of Ni species may serve as the recombination center of photogenerated charges and inhibit the PEC activity [33]. Meanwhile, the incident photon-to-current conversion efficiency (IPCE) was determined (Fig. 5b), and Ni doping could obviously promote the IPCE value. In particular, the IPCE value of 5-Ni-$BiVO_4$ was up to 45% at 400–450 nm, while it was only 25% for pure $BiVO_4$. Similarly, the applied bias photon-to-current efficiency (ABPE) was tested to be 0.55% for 5-Ni-$BiVO_4$ at 0.8 V versus RHE, while only 0.19% for pure $BiVO_4$ (Fig. S2). In addition, 5-Ni-$BiVO_4$ showed good photostability (Fig. 5c).

In electrochemical impedance spectra (EIS), the arc radius of Nyquist plots can be used to evaluate the charge transfer resistance (R_{ct}) at the semiconductor/electrolyte interface, and the smaller arc radius implies lower R_{ct}. The R_{ct} was calculated based on the fitting model, as seen in the inset of Fig. 5d, and the data are shown in Table S1. The R_{ct} was in the order of R_{ct}(5-Ni-$BiVO_4$) < R_{ct}(3-Ni-$BiVO_4$) < R_{ct}(10-Ni-$BiVO_4$) < R_{ct}($BiVO_4$). Obviously, the conductivity of $BiVO_4$ was significantly decreased by Ni doping and surface defects, and 5-Ni-$BiVO_4$ showed the lowest resistivity, consistent with the PEC performances.

Therefore, the optimal Ni doping (5-Ni-$BiVO_4$) can decrease the $BiVO_4$ particle size and form abundant surface V^{4+} and oxygen defects, which then introduces new band levels in the band gap and accelerates the charge transfer [16], benefiting optical absorption, charge separation efficiency, and finally the PEC performance.

Conclusions

We synthesized Ni-doped $BiVO_4$ through an in situ electrodeposition method. The doping can decrease the particle size of $BiVO_4$, and lead to the formation of V^{4+} species and oxygen defects. Accordingly, the doped $BiVO_4$ shows high optical absorption and rapid charge transfer. Therefore, Ni-doped $BiVO_4$ shows a much higher PEC activity than the pure form. Specifically, 5-Ni-$BiVO_4$ exhibits the best PEC performance, with the photocurrent as high as 2.39 mA/cm^2 at 1.23 V versus RHE, a high IPCE (400 nm) value of 45%, and good PEC stability.

Acknowledgements The authors are grateful for the support from the National Natural Science Foundation of China (Nos. 51661145026, 21506156, 21676193) and the Tianjin Municipal Natural Science Foundation (No. 16JCQNJC05200).

References

1. Ji LL, Lv CC, Chen ZF et al (2018) Nickel-based (photo) electrocatalysts for hydrogen production. Adv Mater 30:e1705653
2. Wang YF, Zhang ZY, Shang QQ et al (2018) Synthesis and optimization of TiO_2/graphene with exposed 001 facets based on response surface methodology and evaluation of enhanced photocatalytic activity. Trans Tianjin Univ 24:415–423
3. Wang YF, Zou YL, Shang QQ et al (2018) Quasi-spherical brookite TiO_2 nanostructures synthesized using solvothermal method in the presence of oxalic acid. Trans Tianjin Univ 24:326–339
4. Tan X, Li XL, Yu T et al (2016) Preparation and photocatalytic activity of BiOBr/TiO_2 heterojunction nanocomposites. Trans Tianjin Univ 22:211–217
5. Kim JH, Jo Y, Kim JH et al (2015) Wireless solar water splitting device with robust cobalt-catalyzed, dual-doped $BiVO_4$ photoanode and perovskite solar cell in tandem: a dual absorber artificial leaf. ACS Nano 9:11820–11829
6. Fujishima A, Honda K (1972) Electrochemical photolysis of water at a semiconductor electrode. Nature 238:37–38
7. Walter MG, Warren EL, McKone JR et al (2010) Solar water splitting cells. Chem Rev 110:6446–6473
8. Wang ZL, Lv JL, Zhang JL et al (2018) Facile synthesis of Z-scheme $BiVO_4$/porous graphite carbon nitride heterojunction for enhanced visible-light-driven photocatalyst. Appl Surf Sci 430:595–602
9. Tee SY, Win KY, Teo WS et al (2017) Recent progress in energy-driven water splitting. Adv Sci 4:1600337
10. Kang D, Kim TW, Kubota SR et al (2015) Electrochemical synthesis of photoelectrodes and catalysts for use in solar water splitting. Chem Rev 115:12839–12887
11. Huang ZF, Pan L, Zou JJ et al (2014) Nanostructured bismuth vanadate-based materials for solar-energy-driven water oxidation: a review on recent progress. Nanoscale 6:14044–14063
12. Park Y, Mcdonald KJ, Choi KS (2013) Progress in bismuth vanadate photoanodes for use in solar water oxidation. Chem Soc Rev 42:2321–2337
13. Tang YQ, Wang RR, Yang Y et al (2016) Highly enhanced photoelectrochemical water oxidation efficiency based on triadic quantum dot/layered double hydroxide/$BiVO_4$ photoanodes. ACS Appl Mater Interfaces 8:19446–19455
14. Chen F, Yang Q, Sun J et al (2016) Enhanced photocatalytic degradation of tetracycline by AgI/$BiVO_4$ heterojunction under visible-light irradiation: mineralization efficiency and mechanism. ACS Appl Mater Interfaces 8:32887–32900
15. Qiu YC, Liu W, Chen W et al (2016) Efficient solar-driven water splitting by nanocone $BiVO_4$-perovskite tandem cells. Sci Adv 2:e1501764
16. Wu JM, Chen Y, Pan L et al (2018) Multi-layer monoclinic $BiVO_4$ with oxygen vacancies and V^{4+} species for highly efficient visible-light photoelectrochemical applications. Appl Catal B 221:187–195

17. Saito R, Miseki Y, Sayama K (2012) Highly efficient photoelectrochemical water splitting using a thin film photoanode of $BiVO_4$/SnO_2/WO_3 multi-composite in a carbonate electrolyte. Chem Commun 48:3833–3835
18. Mcdonald KJ, Choi KS (2012) A new electrochemical synthesis route for a BiOI electrode and its conversion to a highly efficient porous $BiVO_4$ photoanode for solar water oxidation. Energy Environ Sci 9:8553–8557
19. Long MC, Cai WM, Kisch H (2008) Visible light induced photoelectrochemical properties of n-$BiVO_4$ and n-$BiVO_4$/p-Co_3O_4. J Phys Chem C 112:548–554
20. Lee MG, Kim DH, Sohn W et al (2016) Conformally coated $BiVO_4$ nanodots on porosity-controlled WO_3 nanorods as highly efficient type II heterojunction photoanodes for water oxidation. Nano Energy 28:250–260
21. Seabold JA, Choi KS (2012) Efficient and stable photo-oxidation of water by a bismuth vanadate photoanode coupled with an iron oxyhydroxide oxygen evolution catalyst. J Am Chem Soc 134:2186–2192
22. Huang MY, Bian JC, Xiong W et al (2018) Low-dimensional Mo: $BiVO_4$ photoanodes for enhanced photoelectrochemical activity. J Mater Chem A 6:3602–3609
23. Yoon KR, Ko JW, Youn DY et al (2016) Synthesis of Ni-based co-catalyst functionalized W: $BiVO_4$ nanofibers for solar water oxidation. Green Chem 18:944–950
24. Nair V, Perkins CL, Lin QY et al (2016) Textured nanoporous Mo: $BiVO_4$ photoanodes with high charge transport and charge transfer quantum efficiencies for oxygen evolution. Energy Environ Sci 9:1412–1429
25. Jovic V, Laverock J, Rettie AJE et al (2015) Soft X-ray spectroscopic studies of the electronic structure of M: $BiVO_4$ (M = Mo, W) single crystals. J Mater Chem A 3:23743–23753
26. Pilli SK, Furtak TE, Brown LD et al (2011) Cobalt-phosphate (Co-Pi) catalyst modified Mo-doped $BiVO_4$ photoelectrodes for solar water oxidation. Energy Environ Sci 4:5028–5034
27. Yao W, Iwai H, Ye J (2008) Effects of molybdenum substitution on the photocatalytic behavior of $BiVO_4$. Dalton Trans 21:1426–1430
28. Luo WJ, Yang ZS, Li ZS et al (2011) Solar hydrogen generation from seawater with a modified $BiVO_4$ photoanode. Energy Environ Sci 4:4046–4051
29. Zhong DK, Choi S, Gamelin DR (2011) Near-complete suppression of surface recombination in solar photoelectrolysis by "Co–Pi" catalyst-modified W: $BiVO_4$. J Am Chem Soc 133:18370–18377
30. Ye H, Lee J, Jang JS et al (2010) Rapid screening of $BiVO_4$-based photocatalysts by scanning electrochemical microscopy (SECM) and studies of their photoelectrochemical properties. J Phys Chem C 114:13322–13328
31. Ye H, Park HS, Bard AJ (2011) Screening of electrocatalysts for photoelectrochemical water oxidation on W-doped $BiVO_4$ photocatalysts by scanning electrochemical microscopy. J Phys Chem C 115:12464–12470
32. Gao B, Wang T, Fan XL et al (2017) Synthesis of yellow mesoporous Ni-doped TiO_2 with enhanced photoelectrochemical performance under visible light. Inorg Chem Front 4:898–906
33. Li J, Wang J, Zhang GK et al (2018) Enhanced molecular oxygen activation of Ni^{2+}-doped BiO_{2-x} nanosheets under UV, visible and near-infrared irradiation: mechanism and DFT study. Appl Catal B 234:167–177
34. Zhou B, Zhao X, Liu HJ et al (2011) Synthesis of visible-light sensitive M-BiVO4 (M = Ag Co, and Ni) for the photocatalytic degradation of organic pollutants. Sep Purif Technol 77(3):275–282
35. Meng WW, Wang L, Li YH et al (2018) Enhanced sensing performance of mixed potential ammonia gas sensor based on $Bi_{0.95}Ni_{0.05}VO_{3.975}$ by silver. Sensors Actuator B Chem 259:668–676
36. Quiñonero J, Gómez R (2017) Controlling the amount of co-catalyst as a critical factor in determining the efficiency of photoelectrodes: the case of nickel (II) hydroxide on vanadate photoanodes. Appl Catal B 217:437–447
37. Kim TW, Choi KS (2014) Nanoporous $BiVO_4$ photoanodes with dual-layer oxygen evolution catalysts for solar water splitting. Science 343:990–994
38. Park HS, Kweon KE, Ye H et al (2011) Factors in the metal doping of $BiVO_4$ for improved photoelectrocatalytic activity as studied by scanning electrochemical microscopy and first-principles density-functional calculation. J Phys Chem C 115:17870–17879
39. Madhusudan P, Ran JR, Zhang J et al (2011) Novel urea assisted hydrothermal synthesis of hierarchical $BiVO_4$/$Bi_2O_2CO_3$ nanocomposites with enhanced visible-light photocatalytic activity. Appl Catal B 110:286–295
40. Li GS, Zhang DQ, Yu JC (2008) Ordered mesoporous $BiVO_4$ through nanocasting: a superior visible light-driven photocatalyst. Chem Mater 20:3983–3992
41. Yu JQ, Kudo A (2006) Effects of structural variation on the photocatalytic performance of hydrothermally synthesized $BiVO_4$. Adv Funct Mater 16:2163–2169
42. Frost RL, Henry DA, Weier ML et al (2006) Raman spectroscopy of three polymorphs of $BiVO_4$: clinobisvanite, dreyerite and pucherite, with comparisons to $(VO_4)^{3-}$ bearing minerals: Namibite, pottsite and schumacherite. J Raman Spectrosc 37:722–732
43. Karunakaran C, Kalaivani S (2015) Synthesis of nanoparticulate in-doped $BiVO_4$ for enhanced visible-light photocatalytic degradation of dye. Int J Appl Ceram Tec 12:711–721
44. Luo B, Liu G, Wang LZ (2016) Recent advances in 2D materials for photocatalysis. Nanoscale 8:6904–6920
45. Wang SC, Chen P, Yun JH et al (2017) An electrochemically treated $BiVO_4$ photoanode for efficient photoelectrochemical water splitting. Angew Chem Int Ed Engl 56:8500–8504
46. Wu QP, Vandekrol R (2012) Selective photoreduction of nitric oxide to nitrogen by nanostructured TiO_2 photocatalysts: role of oxygen vacancies and iron dopant. J Am Chem Soc 134:9369–9375
47. Zhou FQ, Min YL, Fan JC et al (2015) Reduced graphene oxide-grafted cylindrical like W doped $BiVO_4$ hybrids with enhanced performances for photocatalytic applications. Chem Eng J 266:48–55